2014-9

A Simple Solution Method for the Blade Element Momentum Equations with Guaranteed Convergence

Andrew Ning
Brigham Young University - Provo, aning@byu.edu

RESEARCH ARTICLE

A simple solution method for the blade element momentum equations with guaranteed convergence

S. Andrew Ning

National Renewable Energy Laboratory, Golden, CO, 80401

ABSTRACT

The blade element momentum equations, though conceptually simple, can be challenging to solve reliably and efficiently with high precision. These requirements are particularly important for efficient rotor blade optimization that utilizes gradient-based algorithms. Many solution approaches exist for numerically converging the axial and tangential induction factors. These methods all generally suffer from a lack of robustness in some regions of the rotor blade design space, or require significantly increased complexity to promote convergence. The approach described here allows for the blade element momentum equations to be parameterized by one variable: the local inflow angle. This reduction is mathematically equivalent, but greatly simplifies the solution approach. Namely, it allows for the use of one-dimensional root-finding algorithms for which very robust and efficient algorithms exist. This paper also discusses an appropriate arrangement of the equation and corresponding bounds for the one-dimensional search—intervals that bracket the solution and over which the function is well-behaved. The result is a methodology for solving the blade element momentum equations with guaranteed convergence and at a superlinear rate.

KEYWORDS

blade element momentum equations; robust solution methodology; guaranteed convergence

Correspondence

Andrew Ning, NREL, 15013 Denver West Parkway, Golden, CO, 80401.

E-mail: andrew.ning@nrel.gov

NOMENCLATURE

α	local angle of attack $(\phi - \theta)$
γ_i	parameters used in Glauert/Buhl correction
κ	nondimensional axial parameter
κ'	nondimensional tangential parameter
λ_r	local tip-speed ratio
Ω	rotor rotation speed
ϕ	local inflow angle
σ'	local solidity $(Bc/(2\pi r))$

θ	local twist angle
a	axial induction factor
a'	tangential induction factor
B	number of blades
c	local chord
c_d	drag coefficient
c_l	lift coefficient
c_n	normal force coefficient
C_T	thrust coefficient
c_t	tangential force coefficient
F	tip/hub loss factor
$f(\phi)$	residual equation
$f_{PB}(\phi)$	residual equation simplified for the propeller brake region
r	local radial position
Re	Reynolds number
U_∞	freestream velocity
W	local inflow velocity

1. INTRODUCTION

Blade element momentum (BEM) theory is still heavily used in wind turbine conceptual design and initial aerodynamic analysis. It combines a control volume conservation of momentum analysis with a blade sectional analysis [1–3]. Various additions have been used to augment BEM theory and account for neglected physics, such as the effect of a finite number of blades and skewed wakes. However, the fundamental methodology remains largely the same between various implementations. Except in a few restrictive cases, the BEM equations require a numerical solution. The most common approach is to form the BEM equations as a function of two variables, the axial and tangential induction factors, and solve the fixed-point problem $(a, a') = f(a, a')$. This equation is solved through an iterative approach, typically a simple fixed-point iteration scheme or Newton's method. A related approach is to use numerical optimization to minimize the sum of the square of the errors in the induction factors (or in the axial and tangential forces). This can be more robust, but generally converges much slower than a quadratically convergent method like Newton's method.

Recent publications highlight the still existing difficulties in solving the BEM equations. McWilliam and Crawford compared Newton's method to fixed-point iteration using a simplified form of the BEM equations that only included the axial induction factor. They showed that Newton's method was consistently more effective than fixed-point iteration [4]. However, even with Newton's method they demonstrated that every airfoil tested failed to converge in small regions of the design space. Masters et al. proposed a method that combines an initial Monte Carlo simulation with sequential quadratic programming [5]. This approach is more robust, although it is still not guaranteed to always converge and is certainly more computationally complex. Maniaci investigated sources for the convergence issues in the National Renewable Energy

Laboratory (NREL) BEM code WT_Perf [6]. He demonstrated that the singularity that exists at an axial induction factor of $a = 1$ is a cause of convergence difficulty, and developed a heuristic smoothing approach that maintains continuity. Since that modification was incorporated, WT_Perf has undergone continual improvements in robustness [7], but the complexity has increased tremendously and still results in occasional convergence failure reports from its users [8]. Figure 1 diagrams the current convergence strategy in WT_Perf, which relies on a complicated combination of Newton's method, a one-dimensional bounds search, binary search, and careful management of bounds.

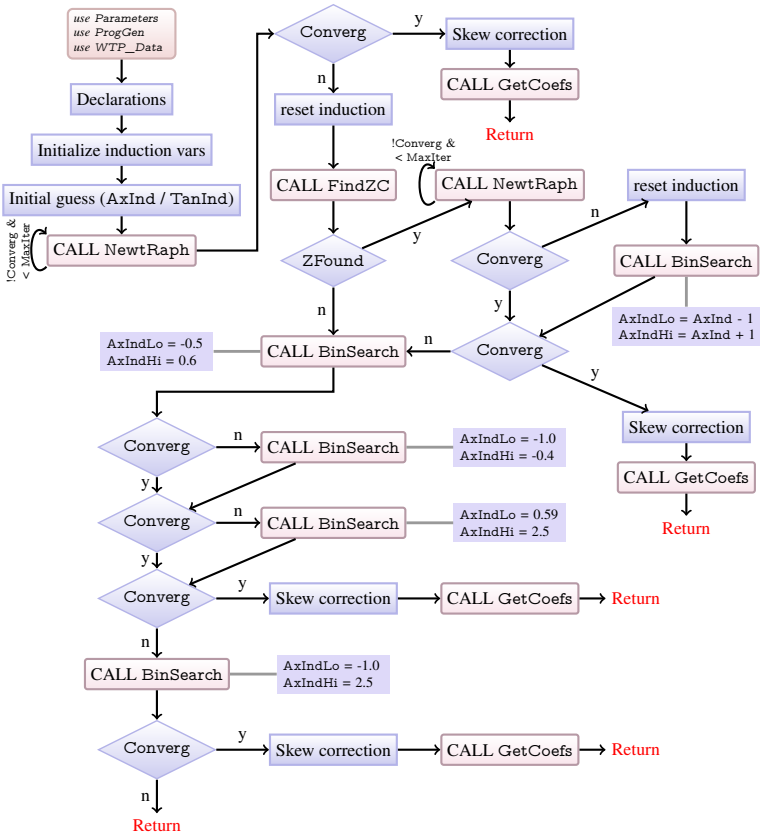

Figure 1. Flowchart of the complex convergence strategy currently used in WT_Perf [7].

While failure to find a solution in certain cases may only be an inconvenience for analysis sweeps or rotor optimization using direct-search algorithms, robustness in solution convergence is critical for other applications such as rotor optimization using gradient-based algorithms. This paper presents a *simple* yet *guaranteed to converge* method to solve the BEM equations. This is accomplished by converting the two-variable, two-equation fixed-point problem into an equivalent one-variable, root-finding problem for which robust algorithms already exist.

2. ONE EQUATION

The main goal of this paper is to reduce the two equations developed from BEM theory into one equation. Equation reduction is a commonly used technique when seeking an analytical solution, but for a large set of equations that are solved numerically, there may not be any advantage to doing so. However, reducing a set of two nonlinear equations to one equation is enormously beneficial. Solving one-dimensional problems is much easier than solving n-dimensional problems (even if n is only two). The key to this reduction is that although two unknowns are always required to specify the inflow

conditions, a great simplification in procedure is possible if the local inflow angle (ϕ) and the magnitude of the local inflow (W) are used as unknowns, rather than the traditional axial and tangential induction factors. Because of the dependence between the variables, this choice allows for a simplification in the solution procedure, whereas using the induction factors does not. If one of the induction factors is used as an unknown, then the local inflow angle cannot be updated without first computing the lift and drag coefficients. However, the lift and drag coefficients are functions of the local inflow angle, thus creating the need for an iterative solution method. Instead, if the local inflow angle is chosen as an unknown, the lift and drag coefficients can be updated without any knowledge of the induction factors. An overview of the algorithm is as follows:

1. Specify the local inflow angle
2. Compute the local angle of attack
3. Estimate the lift and drag coefficients
4. Rotate to rotor plane (compute normal and tangential force coefficients)
5. Compute the induction factors
6. Check the error in the governing equation
7. Try another value of the local inflow angle until the residual approaches zero (using a root-finding method).

The first four steps are straightforward and follow those of the standard method—except for one small potential modification that is discussed in Section 4.1. The fifth step is to estimate the induction factors from the normal and tangential force coefficients. Following the typical procedure, we equate the local thrust coefficient of an annulus of the rotor predicted by sectional theory

$$C_T = \left(\frac{1-a}{\sin\phi}\right)^2 c_n \sigma' \tag{1}$$

to that predicted by momentum theory (with a hub/tip loss correction added)

$$C_T = 4a(1-a)F \tag{2}$$

We then solve for the axial induction factor

$$a(\phi) = \frac{\kappa(\phi)}{1+\kappa(\phi)} \tag{3}$$

where κ is a convenience parameter defined as

$$\kappa(\phi) \equiv \frac{\sigma' c_n(\phi)}{4F(\phi)\sin^2\phi} \tag{4}$$

Note that the induction factor is strictly a function of ϕ. Of course momentum theory is not applicable across all induction factors. If we let β represent the maximum value of the induction factor for which momentum theory is valid (typically between 0.3–0.5 [9]), then equation (3) is valid only for $-1 < \kappa \leq \beta/(1-\beta)$.

For axial induction factors between β and 1.0, momentum theory is invalid and empirical formulas must be used (e.g., Glauert's method). Because one of the goals of this methodology is to allow for use in gradient-based optimization,* the standard Glauert correction is not sufficient when tip/hub loss corrections are used. Buhl [9] derived an approach that maintains C^1 continuity between momentum theory and the empirical correction for cases with tip/hub loss corrections. The thrust coefficient in this range is given by

$$C_T = \left(\frac{50}{9} - 4F\right)a^2 - \left(\frac{40}{9} - 4F\right)a + \frac{8}{9} \tag{5}$$

*If allowing gradient-based optimization is desired, then the lift and drag coefficients should also be parameterized with C^1 continuity. This is typically achieved using spline interpolation in one, two, or three dimensions (i.e., angle of attack, Reynolds number, and thickness-to-chord ratio).

Note that the coefficients reported in Buhl's derivation were for an assumed value of $\beta = 0.4$, although the derivation could be generalized to allow for an arbitrary transition location between the momentum and empirical regions. Including this generality does not affect the conclusions of the following derivation, but it does make the equations more cumbersome. For simplicity, the remainder of the paper uses Buhl's correction with $\beta = 0.4$. It is important to note that the following derivation is only an example and the methodology is not restricted to this particular correction choice. In fact, any description of the axial induction factor can be used as long as it can be parameterized as $a(\phi)$.

Similar to the momentum region, equation (5) is equated to the thrust coefficient predicted by section analysis (1), which yields after simplification

$$a(\phi) = \frac{\gamma_1 - \sqrt{\gamma_2}}{\gamma_3} \tag{6}$$

where

$$\gamma_1 \equiv 2F\kappa - \left(\frac{10}{9} - F\right), \quad \gamma_2 \equiv 2F\kappa - F\left(\frac{4}{3} - F\right), \quad \gamma_3 \equiv 2F\kappa - \left(\frac{25}{9} - 2F\right) \tag{7}$$

This form of the thrust coefficient is valid for $0.4 < a < 1.0$ ($\kappa \geq 2/3$). Care should be taken to avoid the point singularity where the denominator is zero ($\kappa = 25/(18F) - 1$). For that value of κ, the numerator is also exactly zero and the expression is indeterminate. However, if a small number (e.g., 1×10^{-5}) is added or subtracted from κ for this case, then the predicted value for $a(\phi)$ remains finite and introduces negligible error.

The final potential region of interest is for induction factors larger than 1.0, the so-called propeller brake state (see Figure 2). In this region, momentum theory is used with a change in sign

$$C_T = 4a(a-1)F \tag{8}$$

and equating this with sectional theory (1) and solving for a yields

$$a(\phi) = \frac{\kappa(\phi)}{\kappa(\phi) - 1} \tag{9}$$

which is valid for $\kappa > 1$.

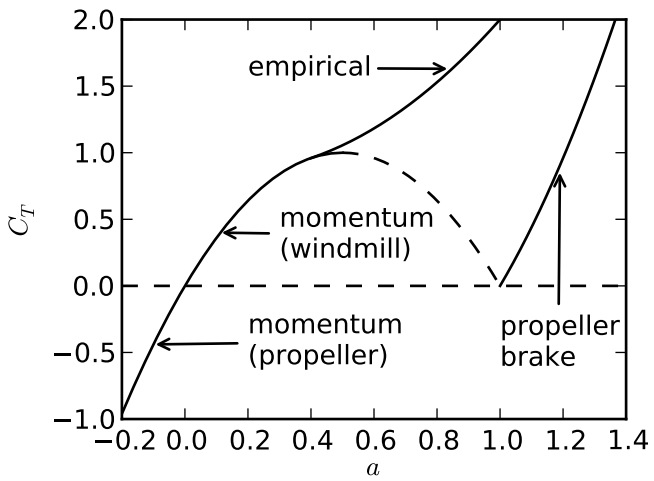

Figure 2. Variation in thrust coefficient with the axial induction factor.

The calculation of the tangential induction factor follows the same procedure by equating torque predicted by momentum and sectional theory. The result is the standard one (but written with a variable substitution for simplification

and to parallel the previous derivation)

$$a'(\phi) = \frac{\kappa'(\phi)}{1 - \kappa'(\phi)} \tag{10}$$

where

$$\kappa'(\phi) \equiv \frac{\sigma' c_t}{4F \sin\phi \cos\phi} \tag{11}$$

Now that the induction factors are specified as functions of the local inflow angle, we can relate the three variables using the geometric relationship between them (Figure 3)

$$\tan\phi = \frac{1 - a}{(1 + a')\lambda_r} \tag{12}$$

This equation can be arranged many different ways to form a residual function, but not all will lead to a reliably convergent method. Singularities in the residual function are unavoidable, but it is convenient to have the quantities $(1 - a)$ and $(1 + a')$ in the denominator so that singularities occur at the predefined locations: $\phi = 0, \pm\pi$. These locations are particularly convenient because they also separate regions where the physics change (e.g., $\phi < 0$ corresponds to the propeller brake region). Note that forcing the singularities to the boundaries, and using the bracketing approach discussed in the following section, avoids the convergence issues associated with singularities that Maniaci demonstrated in the traditional two-dimensional problem [6]. A good choice for forming the residual function is

$$f(\phi) = \frac{\sin\phi}{1 - a} - \frac{\cos\phi}{\lambda_r(1 + a')} = 0 \tag{13}$$

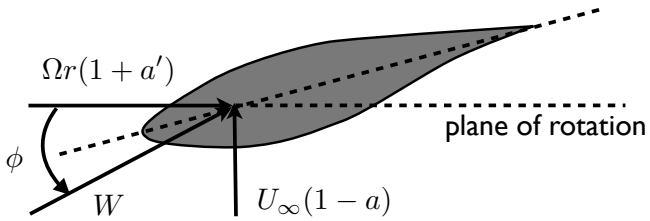

Figure 3. Inflow parameters for a rotating blade section.

We have now reduced the solution approach of the BEM equations from a two-dimensional fixed-point algorithm to a one-dimensional root-finding algorithm. Although the derivation here follows a specific parameterization of the axial induction factor (Glauert/Buhl correction), any method that can be parameterized as $a(\phi)$ will result in a one-equation problem in the same manner. Furthermore, nothing specific to wind turbines has been introduced, and the same fundamental reduction to a one-equation model can be applied to propellers.

3. SOLVING THE REDUCED EQUATION

The advantage of reducing the problem to one dimension is that very robust and efficient one-dimensional root-finding algorithms already exist. For example, Brent's method is one of the best root-finding algorithms for one-dimensional nonlinear functions. It retains the guaranteed convergence properties of bisection (assuming that an initial bracket is given), but converges much faster (superlinearly in most cases) [10]. Thus, if we can bracket a zero of $f(\phi)$ without including any singularities in the interior, then we have solved the problem. This task is made easier by the choice of residual function, which restricts the singularities to the known locations $\phi = 0, \pm\pi$. Any suitable approach can be used to determine a

bracket, and the best approach may differ depending on the application. At the very least, a marching algorithm can be implemented that simply checks for a change of sign. However, this section discusses a more efficient approach where the bracket is determined a priori. The following discussion is specific to the formulations for the axial induction factor introduced in the previous section, and is focused on wind turbine applications. Although the specific results of this section are not generally applicable to other parameterization choices of the axial and tangential induction factors, the approach is. It is also worth emphasizing that this discussion is of secondary importance compared to the more general conclusion already stated—namely that the blade element momentum equations can be reduced to a one-dimensional equation.

Guaranteed convergence for the one-dimensional search depends on bracketing a region that does not contain any singularities in its interior. The residual equation (13) contains singularities at the boundaries between the two solution regions: the momentum/empirical region and the propeller brake region (see Figure 4). Appropriate brackets for solving the BEM equations in each of these two regions are explored in the following sections.

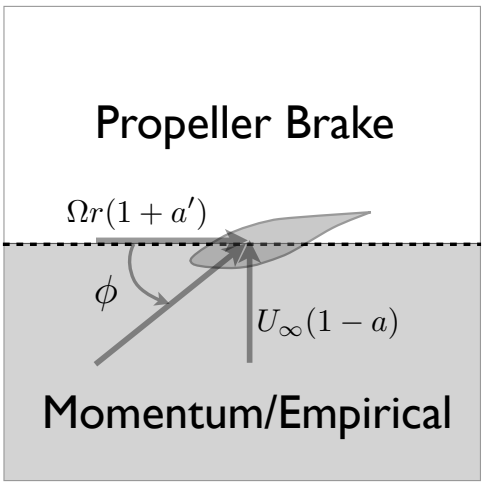

Figure 4. Two half-planes for different solution regions. The momentum/empirical region corresponds to $\phi \in C(0, \pi)$, and the propeller brake region corresponds to $\phi \in C(-\pi, 0)$.

3.1. Momentum/Empirical Region

The momentum/empirical region corresponds to local flow angles in the range $\phi \in C(0, \pi)$ (note that this is an open range to prevent evaluating right at the singularities). The vast majority of solutions for wind turbines are in this range, in particular, most solutions occur in the more restrictive range $(0, \pi/2]$. Solutions yielding local flow angles larger than $\pi/2$ are mathematically possible, but do not typically occur as they correspond to locally reversed tangential flow ($a' < -1$).

As discussed previously, the axial induction factor can be parameterized by $\kappa = \sigma' c_n/(4F \sin^2 \phi)$. Figure 5 shows the range where the different parameterizations of the axial induction factor apply. The propeller brake region does not apply for the range currently being examined. Note that exploring values of κ less than -1 is unnecessary, as a consistent solution to the BEM equations will not be found in that region (other than the trivial solution $\phi = 0, a = 1$, which is always a solution). This can be understood by observing that if κ is negative, then the normal force coefficient must be negative and thus, by (1), the thrust is negative (since $F \geq 0$). Negative thrust is only predicted by the momentum equation. However, equations (1) and (2) never intersect for $\kappa < 1$ (again excluding the trivial solution). This is not to say that negative thrust solutions (negative from the viewpoint of a wind turbine) are not admitted as solutions to this equation. On the contrary, the full domain of the propeller region is captured across the range $-1 < \kappa < 0$. (This curiosity does not occur when using a physical parameter like the axial induction factor. However, for the mathematically convenient parameter κ, not all values are consistent with the physics.)

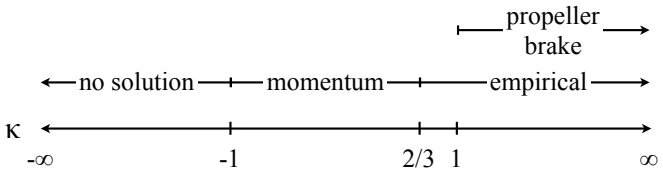

Figure 5. The appropriate method for calculating the axial induction factor based on the value of κ.

There are two possibilities for dealing with the region $\kappa < -1$. The first is to restrict the search for a bracket in the region where $\kappa > -1$. An alternative is to continue using a formulation that does not introduce any artificial solutions. A convenient choice is to continue to use the standard momentum equation for values of $\kappa < -1$. This will lead to predictions of $a > 1$ (propeller brake state) in this region. Because we have limited our range of ϕ from 0 to π, these predictions are not consistent with the BEM equations and do not introduce any artificial solutions (an assertion that is proved below).

Figure 6 shows a typical plot of $f(\phi)$ across the range $(0, \pi/2]$ (the function $f(\phi)$ is usually monotonic or very nearly so in this range. The possibility of multiple solutions is explored in Section 4.3.) The solution point ϕ^*, where $f(\phi^*) = 0$, is indicated in the figure. Also noted is point L, which is defined as the location where $\kappa = -1$ in the range $(0, \pi/2]$. This point represents a lower bound on the feasible region. Values for ϕ below ϕ_L fall in the no-solution region, though we have chosen to continue using the momentum method in that region for convenience. First, we prove that using the momentum method in the no-solution region does not introduce any artificial solutions. Next, we demonstrate that the lower limits of $f(\phi)$ are always negative (both at 0 and at point L, because the values for $f(\phi)$ between 0 and L are artificial). Finally, we discuss the location of an upper bound, such that $f(\phi)$ is positive at the upper bound and thus brackets a zero of $f(\phi)$.

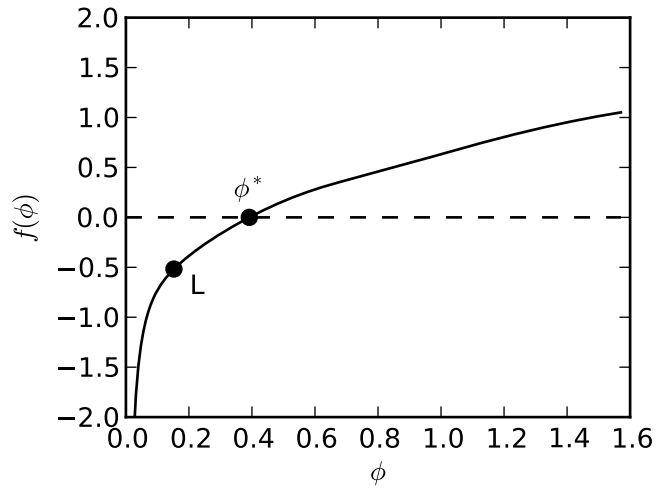

Figure 6. Typical variation in $f(\phi)$ across the range $(0, \pi/2]$. The solution point ϕ^* is shown (where $f(\phi^*) = 0$). Point L corresponds to the point where $\kappa = -1$, and is a lower bound on feasible solutions. The function values $f(\phi)$ for $\phi < \phi_L$ are artificially generated by continuing to use momentum theory.

Theorem 1

No artificial solutions to the residual equation (13) are introduced by continuing to evaluate in the no-solution region; provided that the formulation used in this region always produces axial induction factors larger than 1 (which is true using the momentum method).

$$f(\phi) < 0 \quad \text{for } \phi \in (0, \pi/2] \quad \text{if } \kappa < -1, a > 1 \tag{14}$$

Proof

The no-solution region corresponds to

$$\kappa < -1 \tag{15}$$

Because $\kappa = \sigma' c_n/(4F\sin^2\phi)$, a negative value for κ implies

$$c_n < 0 \tag{16}$$

Using the definition of the normal force coefficient $c_n = c_l\cos\phi + c_d\sin\phi$ and the chosen range implies

$$c_l < 0 \tag{17}$$

In turn, using the definition of the tangential force coefficient $c_t = c_l\sin\phi - c_d\cos\phi$ implies

$$c_t < 0 \tag{18}$$

Using these facts, we can determine a bound on κ' in the no-solution region. The inequality $\kappa < -1$ for the no-solution region can be expressed as

$$\frac{\sigma'}{4F\sin\phi} > \frac{-\sin\phi}{c_n} \tag{19}$$

where the direction of the inequality is switched because $c_n < 0$. Then, using the definition of $\kappa' = \sigma' c_t/(4F\sin\phi\cos\phi)$ and the fact that c_t is negative, we can bound κ' as

$$\kappa' < \frac{-c_t\sin\phi}{c_n\cos\phi} \tag{20}$$

Then, equation (17) can be identically expanded to

$$c_l(\cos^2\phi + \sin^2\phi) + c_d(\cos\phi\sin\phi - \cos\phi\sin\phi) < 0 \tag{21}$$

which can be rearranged as

$$\cos\phi(c_l\cos\phi + c_d\sin\phi) < -\sin\phi(c_l\sin\phi - c_d\cos\phi) \tag{22}$$

Dividing this inequality through by $c_n\cos\phi$ and switching directions of the inequality because c_n is negative (16) yields

$$\frac{-c_t\sin\phi}{c_n\cos\phi} < 1 \tag{23}$$

and thus from (20) we see that

$$\kappa' < 1 \tag{24}$$

The second term of the residual equation (13) can always be expressed as

$$-\frac{\cos\phi(1-\kappa')}{\lambda_r} \tag{25}$$

which for $\kappa' < 1$ will always be negative. The first term of the residual equation, $\sin\phi/(1-a)$, will be negative for any formulation that results in a value of $a > 1$ (e.g., set $a = 1.5$). However, using the momentum calculation is convenient because it allows for a smooth variation in a as a function of κ, which should generally allow for a more efficient solution

of $f(\phi) = 0$. The momentum calculation always predicts values of $a > 1$ for $\kappa < -1$. Thus, the no-solution region will always evaluate to

$$f(\phi) < 0 \quad \text{for } \phi \in (0, \pi/2] \quad \text{if } \kappa < -1 \tag{26}$$

Because no change of sign in the residual function can occur in the no-solution region using this methodology, no artificial solutions can be introduced. □

Theorem 2

The value of the residual function at the boundary between the no-solution region and the momentum region is always negative

$$f(\phi_L) < 0 \tag{27}$$

Proof

At point L (see Figure 6), $\kappa = -1$. Because $\sin\phi$ is finite at point L, the first term in the residual function (13) is zero

$$\frac{\sin\phi}{1-a} = \sin\phi(1+\kappa) = 0 \tag{28}$$

Borrowing the results of the previous proof, at point L the inequality from (20) results in the equality

$$\kappa' = \frac{-c_t \sin\phi}{c_n \cos\phi} \tag{29}$$

and thus by equation (23)

$$\kappa' < 1 \tag{30}$$

This makes the second term in the residual function (13) negative

$$-\frac{\cos\phi(1-\kappa')}{\lambda_r} < 0 \tag{31}$$

and thus

$$f(\phi_L) < 0 \tag{32}$$

□

Theorem 3

At the lower bound of 0, the residual function is always negative.

$$\lim_{\phi \to 0^+} f(\phi) = -\infty \tag{33}$$

Proof

The previous two proofs show that the residual function is negative both at point L and between point L and the lower boundary 0. However, point L does not always exist (i.e., κ does not always go below -1 in the range $\phi \in (0, \pi/2]$). In this case, we can prove that the residual function is still negative at the lower bound ($\phi \to 0^+$). If point L does not exist, then

$$\lim_{\phi \to 0} \kappa(\phi) = +\infty \tag{34}$$

(If κ were approaching $-\infty$, then point L would exist). For this value of κ, the empirical (Glauert/Buhl) correction applies (6). Even after simplification the first term in the residual function (13) yields an indeterminate form $0/0$ at the lower limit.

Using L'Hôpital's rule

$$\lim_{\phi \to 0^+} \frac{\sin\phi}{1-a} = \lim_{\phi \to 0^+} \frac{\cos\phi}{-da/d\phi} = \frac{1}{-da/d\phi(0)} \tag{35}$$

At $\phi = 0$, $da/d\phi$ is finite and negative for the empirical region. Thus, the first term in the residual equation is positive and finite.

Using the definition of κ' (11), we can show that

$$\lim_{\phi \to 0^+} \kappa' = -\frac{\sigma' c_d}{4F\sin\phi} = -\infty \tag{36}$$

since c_d is always positive. Thus, the second in the residual function (13) approaches

$$\lim_{\phi \to 0^+} -\frac{\cos\phi}{\lambda_r(1+a')} = \lim_{\phi \to 0^+} -\frac{(1-\kappa')}{\lambda_r} = -\infty \tag{37}$$

Adding these two terms, we see that

$$\lim_{\phi \to 0^+} f(\phi) = -\infty \tag{38}$$

This limit still holds even if $\phi = 0$ falls into the no-solution region $\kappa < -1$. The first term in the residual equation evaluates to

$$\lim_{\phi \to 0^+} \frac{\sin\phi}{1-a} = \lim_{\phi \to 0^+} \sin\phi(1+\kappa) = \lim_{\phi \to 0^+} \left(\sin\phi + \frac{\sigma' c_n}{4F\sin\phi}\right) = -\infty \tag{39}$$

(because c_n is negative for $\kappa < -1$). The second term in the residual function is unchanged and approaches $-\infty$. Thus, in either case, the lower limit always holds for this formulation

$$\lim_{\phi \to 0^+} f(\phi) = -\infty \tag{40}$$

□

These three proofs demonstrate that $f(0)$ is always negative. Furthermore, the first proof demonstrates that continuing to use the momentum method into the no-solution region has no effect on the solution, but is more efficient because it does not require solving a second one-dimensional equation to determine a new lower limit.

At the upper limit, $f(\pi/2)$ is almost always positive. However, because some exceptions exist, a rigorous proof is not available. The value of κ at the upper boundary is

$$\kappa(\phi = \pi/2) = \frac{\sigma' c_d}{4F} \tag{41}$$

which is always positive and finite. Thus, depending on the magnitude of κ, either the momentum region or empirical region applies (Figure 5). The smallest value $f(\pi/2)$ can reach is in the momentum region (in the empirical region the first term is even larger and positive), and after simplification has the value

$$f(\pi/2) = 1 + \frac{\sigma' c_d}{4F} + \frac{\sigma' c_l}{4F\lambda_r} \tag{42}$$

Both force coefficients are evaluated at the angle of attack $\alpha = \pi/2 - \theta$. For positive twist angles, the lift coefficient should be positive, and thus $f(\pi/2)$ is positive. Even for modest negative twist angles the angle of attack is still close to $90°$, where the drag coefficient is near its maximum and the lift coefficient is small in magnitude. In these cases, the sum of the second and third term may be slightly negative, but still generally much smaller than 1. For the vast majority of cases,

$f(\pi/2)$ is close to 1. However, it is possible for $f(\phi)$ to be negative, for example, if κ is in the momentum region and

$$c_l < -\lambda_r \left(\frac{4F}{\sigma'} + c_d \right) \tag{43}$$

This could occur, for example, for sections with low tip-speed ratios and significant negative twist angles. For these cases, a solution does not exist in the range of $(0, \pi/2]$ (but a solution *does exist* in a different range, as discussed below).

We can test if a solution will exist in the range $(0, \pi/2]$ simply by evaluating $f(\phi)$ at $\pi/2$. If the value is positive, then we can safely use the bounds $(0, \pi/2]$. If the value is not positive, then two alternatives exist: search for a solution in the range $\phi \in [\pi/2, \pi)$, or search for a solution in the propeller brake region. Let us first consider solutions in the range $\phi \in [\pi/2, \pi)$. The behavior of $f(\phi)$ in this range will not be described with the same rigor as what was described for the main range of $(0, \pi/2]$. This is primarily because these solutions are generally of little interest as they correspond to locally reversed tangential flow, but also because the rigorous proofs shown earlier in this section do not hold for all cases in this region. However, we can easily show that if a solution does not exist in the range $\phi \in (0, \pi/2]$, then a solution is guaranteed to exist in $\phi \in [\pi/2, \pi)$. This is proven by showing that the upper boundary of this region produces a positive residual value.

Theorem 4
If κ passes into the no-solution region as $\phi \to \pi$ (let us define point U as the point where $\kappa = -1$ in the range $[\pi/2, \pi)$) then

$$f(\phi_U) > 0 \tag{44}$$

The proof follows the procedure outlined for Theorem 2. Values of $f(\phi)$ for $\phi > \phi_U$ are artificial.

Theorem 5
If point U does not exist, then the upper boundary approaches $+\infty$

$$\lim_{\phi \to \pi^-} f(\phi) = +\infty, \quad \text{if } c_l(\pi - \theta) < 0 \tag{45}$$

The steps of this proof are the same as for Theorem 3.

In either case, the residual function at the upper boundary is positive. Thus, if the first bracket does not contain a solution (i.e., $f(\pi/2) < 0$), then the bracket $[\pi/2, \phi_U)$ (or $[\pi/2, \pi)$ if point U does not exist) is guaranteed to bracket a solution to $f(\phi)$. In practice, using π as an upper limit for this bracket works well, but because a proof analogous to that for Theorem 1 does not hold, one should find point U (by solving the one-dimensional equation $\kappa(\phi) = -1$) and use ϕ_U as an upper boundary (to be safe).

The second (and typically better) option for when the main bracket does not contain a solution ($f(\pi/2) < 0$), is to search for a solution in the propeller brake region. Although we are mathematically guaranteed to find a solution in $\phi \in C(0, \pi)$, the more physically likely solution may exist in the propeller brake region. This region is discussed in the following section.

3.2. Propeller Brake Region

The propeller brake region corresponds to local flow angles in the range $\phi \in C(-\pi, 0)$. Similar to the momentum/empirical region, physically realizable solutions are likely to occur in a much more restrictive range. We will focus on solutions within the range $[-\pi/4, 0)$ for wind turbines, but like the previous section we can extend the bracket all the way to the lower boundary if necessary.

For this range of local flow angles, the momentum and empirical regions can be ignored. Because only the propeller brake calculation for the axial induction factor applies, the residual equation can be simplified as follows

$$f_{PB}(\phi) = \sin\phi(1 - \kappa) - \frac{1}{\lambda_r} \cos\phi(1 - \kappa') \tag{46}$$

where this equation is applicable for $\kappa > 1$. Following the same logic as the previous section, we will continue to use the propeller brake calculation even for $\kappa < 1$ as long as it does not introduce artificial solutions. A typical curve for f_{PB}, shown for a wind turbine with significant negative pitch, is shown in Figure 7. Below point M, the propeller brake equation no longer applies (i.e., $\kappa < 1$). To bracket a solution, we need to show that the function is negative at the lower bound and at point M, and that the function is positive as $\phi \to 0^-$.

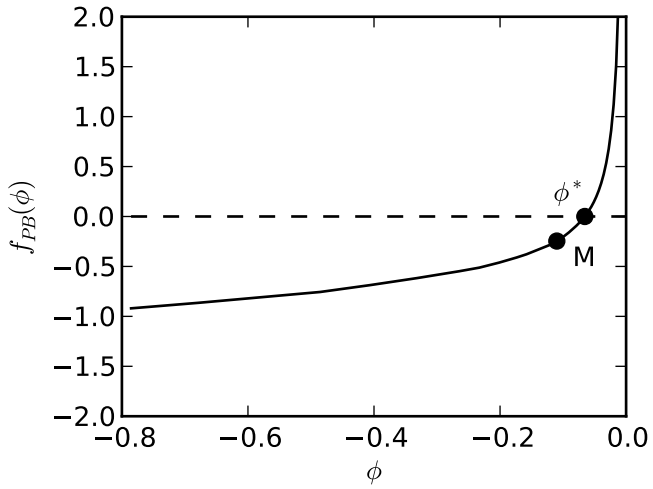

Figure 7. Characteristic plot of $f_{PB}(\phi)$ across the range $[-\pi/4, 0)$. The solution point ϕ^* is shown (where $f_{PB}(\phi^*) = 0$). Point M corresponds to the point where $\kappa = 1$, and is a lower bound on feasible solutions. The function values $f_{PB}(\phi)$ for $\phi < \phi_M$ are artificial and only used for convenience.

Theorem 6

Point M is defined as the location where $\kappa = 1$ in the range $\phi \in [-\pi/4, 0)$. If this point exists, then

$$f_{PB}(\phi_M) < 0 \tag{47}$$

Proof

The first steps of the proof are omitted, as they parallel the proof of Theorem 2. Following the outlined steps, we can show that

$$f_{PB}(\phi_M) < 0, \quad \text{if } c_l > -c_d \tan(2\phi_M) \tag{48}$$

However, we also know that at point M, $c_n > 0$ (since $\kappa = 1$). This implies that

$$c_l > -c_d \tan \phi_M \tag{49}$$

Across the range $[-\pi/4, 0)$, $\tan\phi$ is always larger than $\tan(2\phi)$. Thus, if point M exists in this range, then

$$f_{PB}(\phi_M) < 0 \tag{50}$$

□

The upper and lower limit are not subject to a mathematical proof as their sign may change according to the conditions. At the upper limit of $\phi = 0$

$$\lim_{\phi \to 0^-} f_{PB}(\phi) = -\frac{\sigma'}{4F \sin\phi}(c_l + \frac{c_d}{\lambda_r}) - \frac{1}{\lambda_r} \tag{51}$$

As we approach zero from below, the term $\sin\phi$ is very small and negative. Thus, the function approaches $+\infty$ if the term in parenthesis is positive, namely if

$$c_l(-\theta) > -\frac{c_d(-\theta)}{\lambda_r} \tag{52}$$

Searching for a solution in the propeller brake region implies that a solution in the main region could not be found. This occurs only if c_l is strongly negative at $\phi = \pi/2$ (see equation (42)). The aerodynamics of an airfoil suggest that the lift coefficient changes sign approximately every 90 degrees. Because the lift coefficient of this section is strongly negative at $\phi = \pi/2$, then the lift coefficient at $\phi = 0$ is almost certainly positive. Thus, this upper limit should be positive (i.e., $c_l(-\theta) > 0 \Rightarrow \lim_{\phi \to 0^-} f_{PB}(\phi) = +\infty$). However, this is not a mathematical proof, and there is no harm in simply checking the sign of $f_{PB}(\phi)$ at the upper bound numerically.

At the chosen lower limit ($\phi = -\pi/4$), the function evaluates to

$$f_{PB}(-\pi/4) = \left(1 + \frac{1}{\lambda_r}\right)\left[-\frac{\sqrt{2}}{2} + \frac{\sigma'}{4F}\left(c_l + c_d\left(\frac{1-\lambda_r}{1+\lambda_r}\right)\right)\right] \tag{53}$$

The $-\sqrt{2}/2$ term tends to dominate in magnitude over the other two terms in the bracket, leading to a negative value for the function. The lower limit of $-\pi/4$ was chosen somewhat arbitrarily, though it is a physically realistic range and is necessary to prove Theorem 6. A more negative lower bound can certainly be used, however, any solutions would need to be numerically verified to not be artificial (i.e., ensure that $\kappa > 1$).

3.3. Solution Algorithm

The presented proofs have shown that, for the chosen residual function and implementation of $a(\phi)$, a suitable root-finding algorithm will *always* converge to a solution of the BEM equations. Furthermore, the appropriate bracket can be determined simply—with only one function call for the vast majority of cases. The specific details of this section are based on a particular choice for the parameterization of $a(\phi)$ and other corrections to the BEM model. Other parameterizations will still allow for a one-dimensional root-finding algorithm, but not all theorems of this section may be valid. This just means that, for an arbitrary parameterization, appropriate brackets may need to be found numerically (e.g., check that $f(0) < 0$ rather than rely on the mathematical proof). However, the general behavior of $f(\phi)$, the bracketing strategy, and the priority of which ranges to search first should be broadly applicable for wind turbine applications.

An algorithm for solving the BEM equations using the chosen formulation of $a(\phi)$ is summarized below. In this algorithm, it is assumed that the most likely solution falls in the range $(0, \pi/2]$, and indeed this is almost always the case. If such a solution does not exist, then one is sought in the propeller brake region. As was discussed in the previous section, the mathematics along with the airfoil aerodynamics suggest (not a mathematical proof) that if a solution does not exist for $\phi \in (0, \pi/2]$, then one almost certainly exists in the propeller brake region. As a last resort, the solution for $\phi \in [\pi/2, \pi)$ is found. Here, a mathematical proof is available, suggesting that if a solution could not be found for $\phi \in (0, \pi/2]$, then a solution is guaranteed to exist for $\phi \in [\pi/2, \pi)$.

Algorithm 1 determine solution ϕ^* to BEM equations

function $zero(f, lb, ub)$ ▷ e.g., Brent's method
  return x^* where $f(x^*) = 0$ for $lb < x < ub$ and $f(lb)f(ub) < 0$

function $a(\phi)$ ▷ only used for $f(\phi)$
  if $\kappa < 2/3$ **then**
    $a \leftarrow \kappa/(1+\kappa)$
  else
    $a \leftarrow (\gamma_1 - \sqrt{\gamma_2})/\gamma_3$
  return a

function $f(\phi)$
  return $\sin\phi/(1-a(\phi)) - \cos\phi(1-\kappa'(\phi))/\lambda_r$

function $f_{PB}(\phi)$
  return $\sin\phi(1-\kappa(\phi)) - \cos\phi(1-\kappa'(\phi))/\lambda_r$

function BEMSOLVE
  $\epsilon \leftarrow 1 \times 10^{-6}$ ▷ or some other suitably small value
  if $f(\pi/2) > 0$ **then** ▷ this is almost always true
    $\phi^* \leftarrow zero(f(\phi), \epsilon, \pi/2)$
  else if $f_{PB}(-\pi/4) < 0$ and $f_{PB}(\epsilon) > 0$ **then** ▷ propeller brake region
    $\phi^* \leftarrow zero(f_{PB}(\phi), -\pi/4, -\epsilon)$
  else ▷ if all else fails, this is guaranteed to contain a solution
    $\phi^* \leftarrow zero(f(\phi), \pi/2, \pi)$
  $a \leftarrow a(\phi^*)$
  $a' \leftarrow a'(\phi^*)$

4. ADDITIONAL CONSIDERATIONS

4.1. Reynolds Number

Section 2 introduced the idea of specifying the inflow through the local inflow angle (ϕ) and the local inflow velocity (W), as opposed to the traditional induction factors. The benefit of this approach is that in each step of the algorithm the equations can be specified strictly as a function of ϕ, whereas the other unknown W is not directly needed. However, there is a case where the magnitude of the local inflow velocity is directly needed, and that occurs when Reynolds number dependence is included in the airfoil model. Fortunately, the methodology allows for precise Reynolds number dependence to be included by adding one modification.

In the computation of $a(\phi)$ and $a'(\phi)$, the inflow velocity must be computed in order to estimate the local Reynolds number. The inflow velocity is given by

$$W = \sqrt{U_\infty^2(1-a)^2 + (\Omega r)^2(1+a')^2} \tag{54}$$

However, the induction factors are not yet known and so the inflow velocity cannot be directly computed. The simplest option to resolve this is to ignore the induction factors for the purpose of computing the Reynolds number ($W = \sqrt{U_\infty^2 + (\Omega r)^2}$). However, if desired, the Reynolds number can also be computed exactly (within a given tolerance) through internal iteration. After the initial computation, the newly computed induction factors can be used again in Equation (54) to re-compute the inflow velocity and subsequently re-compute the induction factors. As discussed below, at most only one additional iteration is necessary to achieve high accuracy, but additional iterations could be used as desired to ensure a specified convergence tolerance for the Reynolds number. This iteration loop happens internally within the computation of $a(\phi)$ and $a'(\phi)$ and does not change the overall algorithm.

The impact of converging the Reynolds number exactly versus using an approximation to avoid extra iterations was assessed using the S815 Clean airfoil [11]. The BEM equations were solved repeatedly on a 200 x 200 x 200 grid for tip-speed ratios from 0.5 to 12, local solidities from 0.005 to 0.1, and local twist angles from -5 to 25 degrees. The freestream Reynolds number was set such that the local Reynolds number spanned the variation in Reynolds number defined for the S815 airfoil. The approximate solutions considered the cases of using only one iteration (assuming $W = \sqrt{U_\infty^2 + (\Omega r)^2}$), as well as using two and three iterations with the updated induction factors. The "exact" solution was found by iterating until the Reynolds number was converged to the nearest whole number (at least 6 or 7 significant figures). Errors were reported relative to the magnitude of the terms used in the inflow velocity calculation ($(1-a)$ and $(1+a')$ or equivalently the error in axial and tangential velocity) so as not to exaggerate small differences between very small numbers. Figure 8 shows both the mean and maximum errors in the 8 million simulations as a function of the number of internal iterations on Reynolds number. Even when the induction factors are ignored in the Reynolds number calculation, the average error in the axial component of velocity is only 0.0048%. In all cases, the error in the tangential component of velocity is less than the error in the axial component. Figure 8b shows that the maximum error can be significant with only one iteration (2.3% for $(1-a)$), but it turns out that such significant errors are extremely rare. Table I summarizes what percentage of the 8 million simulations achieve certain error levels. We see that even if no additional iterations on Reynolds number are used, 99.96% of the simulations produced less than 1% error for the axial component of velocity. Adding just one additional iteration achieves an error level less than 0.01% for 99.55% of the samples.

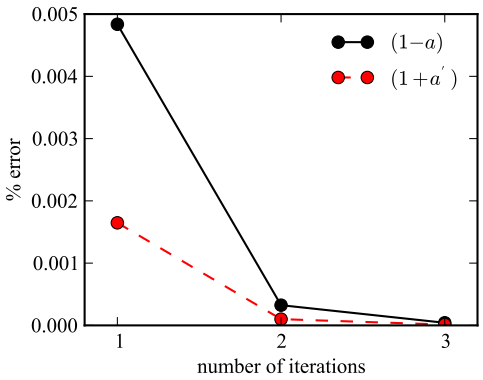

(a) Mean percent error in $(1-a)$ and $(1+a')$.

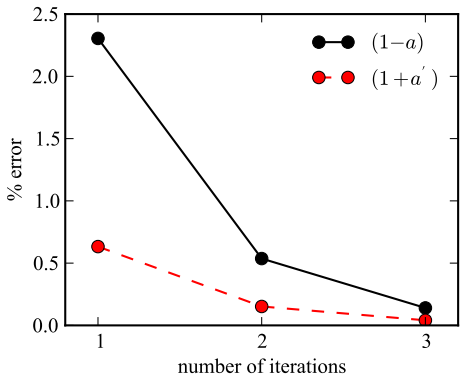

(b) Maximum percent error in $(1-a)$ and $(1+a')$.

Figure 8. Mean and maximum errors in the velocity components across 8 million simulations as a function of the number of internal iterations.

Table I. Percent error in $(1-a)$ relative to using an exact value for the Reynolds number across 8 million simulation cases.

	1 iteration	2 iterations	3 iterations
% of simulations that have less than 1% error	99.96%	100%	100%
% of simulations that have less than 0.1% error	98.94%	99.92%	99.998%
% of simulations that have less than 0.01% error	95.42%	99.55%	99.90%

The data suggests that ignoring extra iterations on Reynolds number entirely, or even better, using the induction factors from the previous section, should be sufficient for most applications. The sensitivity of airfoil performance to Reynolds number generally operates on a significantly larger scale than the uncertainty of the inflow velocity due to neglecting the induction factors (especially given the level of uncertainty already inherent in including viscous effects in a strip-wise manner). But, if capturing many significant figures in the Reynolds number is crucial for the application, this can certainly be accomplished and generally with only one additional internal iteration.

4.2. Excluding Drag

Whether or not drag should be included in the prediction of the induction factors is debatable. Wilson et al. argued that drag has little, if any, effect on induced forces, and thus should not be included in computing the induction factors [12]. The discussion on bracketing a solution to the BEM equations in Section 3 is applicable for $c_d = 0$, with one modification. Theorem 3 ($\lim_{\phi \to 0^+} f(\phi) = -\infty$) depends on c_d being nonzero (see equation (36)). If $c_d = 0$ and point L does not exist (see Figure 6), then

$$\lim_{\phi \to 0^+} f(\phi) = -\frac{1}{da/d\phi(0)} - \frac{1}{\lambda_r}\left(1 + \frac{\sigma' c_l}{4F}\right) \tag{55}$$

The sum of these two terms is generally negative, but is not guaranteed to be so. If drag is excluded from computing the induction factors, then the lower limit of 0 cannot be relied upon a priori. Instead, a bracket should be determined numerically.

4.3. Multiple Solutions

This discussion has implicitly assumed that $f(\phi)$ monotonically increases across the various ranges of interest. The derivative of $f(\phi)$ is

$$\frac{df}{d\phi} = \frac{\cos\phi}{1-a} + \frac{\sin\phi}{(1-a)^2}\frac{da}{d\kappa}\frac{d\kappa}{d\phi} + \frac{\sin\phi}{\lambda_r(1+a')} + \frac{\cos\phi}{\lambda_r(1+a')^2}\frac{da'}{d\kappa'}\frac{d\kappa'}{d\phi} \tag{56}$$

A term-by-term examination suggests that the gradient is almost always positive across the primary range of $(0, \pi/2]$. However, for some airfoils, the gradient can reverse signs near $f(0)$ and introduce multiple solutions. McWilliam and Crawford demonstrated the existence of multiple solutions for several airfoil types [4]. One of the more egregious cases was for the rough S815 airfoil. However, the existence of multiple nearby solutions can generally be eliminated by fitting the airfoil data with a spline using a small amount of smoothing. The raw data and spline fits for the S815 airfoil at a Reynolds number of 1×10^6 [11] are compared in Figure 9. Agreement is high except in areas of high-frequency variation. Using this airfoil section, a three-dimensional sweep was conducted on the same 200 x 200 x 200 grid used earlier where the local tip-speed ratio varies from 0.5 to 12, the local solidity from 0.005 to 0.1, and the twist from -5 to 25 degrees. Consistent with the findings in McWilliam and Crawford's paper, if the raw data is used with linear interpolation, then three solutions exist across some sections of the design space. However, when the simulation was repeated using a two-dimensional spline interpolation of the lift and drag coefficients, only one solution existed for every point sampled in the parameter space (specifically a bivariate B-spline interpolation across Reynolds number and angle of attack was used, with a smoothing factor of 0.1 for the lift and 0.001 for the drag).

Although some of the variation missed by using a spline may be physical, usually most of it is not and is introduced by other experimental sources or numerical noise. High-frequency variation that is physics-based resides in regions of high uncertainty, and the existence of multiple solutions in these regions is not surprising given the limitations of the BEM model. To be clear, it is not necessary to fit the airfoil data for applications where that would be undesirable. The method described in this paper is still guaranteed to find a solution, but in the case of multiple solutions, there is no guarantee which solution is found. However, for the purposes of gradient-based optimization, a C^1 continuous spline interpolation is necessary anyway, and a slight approximation in airfoil data is consistent with the goals of conceptual design. This smoothing of airfoil data can be useful in removing many of the occurrences of multiple solutions.

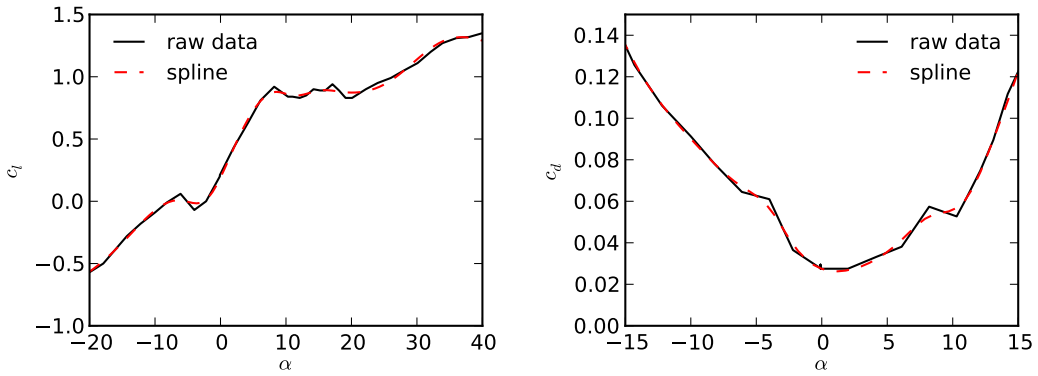

(a) comparison between lift coefficients

(b) comparison between drag coefficients

Figure 9. Lift and drag curves for the rough S815 airfoil as a function of angle of attack, showing both the raw data and a spline interpolation.

4.4. Comparison with Traditional Root-Finding Methods

The robustness and convergence speed of the present method was compared with several alternatives that are typically used for general root-finding or fixed-point problems. Five alternative approaches were examined: basic fixed-point iteration, Newton's method, Steffensen's method, Powell's hybrid algorithm, and the Levenberg-Marquardt algorithm.

All of the alternative algorithms utilize the BEM equations in the form where the induction factors are treated as the unknowns and are updated as

$$(a_{new}, a'_{new}) = f_{BEM}(a, a') \tag{57}$$

Fixed-point iteration is the most straightforward method and simply uses the updated values of the induction factor as the starting point for the next iteration.

$$(a_{i+1}, a'_{i+1}) = f_{BEM}(a_i, a'_i) \tag{58}$$

Iteration is repeated until a convergence criteria is met. The next three methods are all different approaches to finding the roots of the vector function

$$f_{vector} = \begin{bmatrix} (a_{new} - a)^2 \\ (a'_{new} - a')^2 \end{bmatrix} \tag{59}$$

Newton's method requires the Jacobian, which in this case was estimated using one-sided finite differences with a step size of 1×10^{-8}. Steffensen's method is similar to Newton's method and also converges quadratically, but has the advantage of not requiring derivatives. Powell's method is also similar to Newton's method but uses a rank-1 method to update the Jacobian rather than finite-differencing. A forward-difference approximation is used only to initialize the Jacobian or for steps where the rank-1 method performs poorly. Powell's method also does not necessarily take a full Newton step but uses a combination of the Newton step and a scaled gradient step. The implementation used in this simulation came from MINPACK.[†] Finally, the Levenberg-Marquardt algorithm is an optimization approach that minimizes $||f_{vector}||_2$ by using a combination of gradient-descent and a modified version of Newton's method for minimization. Its implementation was also contained in MINPACK.

All six methods were compared across a wide range of local tip-speed ratios (0.5 to 12), local solidities (0.005 to 0.1), and local twist angles (-5 to 25 degrees) on a 20 x 20 x 20 grid. Furthermore, evaluation on this full grid was repeated for each of the 20 airfoils whose names, experimental data sources, and tested Reynolds numbers are summarized in Table II. The first six airfoils came from a Dutch Offshore Wind Energy Converter (DOWEC) 6-MW design [13] (the

[†]More J, Garbow B, Hillstrom K. MINPACK, http://www.netlib.org/minpack/, March 1980, accessed January 2013.

same airfoils used in the NREL 5-MW reference model [14]). Five of these airfoils (DU-W-405LM, DU-W-350, DU-97-W-300LM, DU-91-W2-250LM, DU-93-W-210LM) came from two-dimensional experimental data obtained at the Delft University of Technology [13]. The sixth airfoil is a NACA 64-618, for which experimental data came from Abbott and Von Doenhoff [15]. The next four airfoils came from Risø's Wind Turbine Airfoil Catalogue [16] and include the NACA 63-215, Risø-A1-18, Risø-A1-21, and the Risø-A1-24. Data for these airfoils were obtained in the Velux wind tunnel [17, 18]. The final 10 airfoils included the S801, S810, S813, S815, and S825, which were each tested both with and without leading-edge grit roughness (LEGR) to simulate surface irregularities. Their experimental data were collected at The Ohio State University Aeronautical and Astronautical Research Laboratory [11, 19–22]. For all 20 airfoils, three-dimensional rotational corrections were applied using the Du-Selig method [23] for lift and the Eggers method [24] for drag. The force coefficients were then extrapolated to $\pm 180^\circ$, using Viterna's method [25].

For each combination of tip-speed ratio, solidity, and twist angle, the freestream velocity and chord were set such that the freestream Reynolds number was 0.75×10^6. This value was chosen so that the local Reynolds number would range from about 0.5 to 9 million, and thus cover the span of Reynolds numbers included in the airfoil data. It was assumed in each simulation that the radial station of interest was near the middle of the blade, or in other words, hub and tip losses were assumed negligible so that each simulation would be more directly comparable.

Table II. List of airfoils used in convergence comparison study.

Airfoil Name	Wind Tunnel Data Source	Re $(\times 10^6)$
DU-W-405LM	Delft University of Technology	7
DU-W-350	Delft University of Technology	7
DU-97-W-300LM	Delft University of Technology	7
DU-91-W2-250LM	Delft University of Technology	7
DU-93-W-210LM	Delft University of Technology	7
NACA 64-418	Abbott and Von Doenhoff	6
NACA 63-215	Risø National Laboratory	1.1
Risø-A1-18	Risø National Laboratory	1.6
Risø-A1-21	Risø National Laboratory	1.6
Risø-A1-24	Risø National Laboratory	1.6
S801 Clean	The Ohio State University	0.75, 1.0, 1.25, 1.5
S801 LEGR	The Ohio State University	0.75, 1.0, 1.25, 1.5
S810 Clean	The Ohio State University	0.75, 1.0, 1.25, 1.5
S810 LEGR	The Ohio State University	0.75, 1.0, 1.25, 1.5
S813 Clean	The Ohio State University	0.75, 1.0, 1.25, 1.4
S813 LEGR	The Ohio State University	0.75, 1.0, 1.25, 1.4
S815 Clean	The Ohio State University	0.75, 1.0, 1.25, 1.4
S815 LEGR	The Ohio State University	0.75, 1.0, 1.25, 1.4
S825 Clean	The Ohio State University	0.75, 1.0, 1.25
S825 LEGR	The Ohio State University	0.75, 1.0, 1.25

All algorithms were considered converged when both induction factors were found to within 1×10^{-8} (or for the present one-dimensional method, when the local flow angle was found to within that same tolerance). For the present one-dimensional method, the initial bounds were set at $\phi \in (0, \pi/2]$. Because some of the two-dimensional methods are particularly sensitive to the starting point, each of these simulations was repeated using five judiciously-chosen starting points. The first starting point assumed no knowledge: $a = 0, a' = 0$. The second starting point set the axial induction factor to the optimal value for maximum power production ($a = 1/3, a' = 0$). The third starting point added the optimal tangential induction factor assuming no losses [3]

$$a = \frac{1}{3}, \quad a' = \frac{2}{9\lambda_r^2} \tag{60}$$

The fourth starting point reset the tangential induction factor to zero and used an approximate analytic solution for the axial induction factor using the specific blade geometry and operational point (ignoring losses and using a small angle approximation) [26]

$$a = \frac{1}{4}\left[2 + \pi\lambda_r\sigma' - \sqrt{4 - 4\pi\lambda_r\sigma' + \pi\lambda_r^2\sigma'(8\theta + \pi\sigma')}\right] \tag{61}$$

The final starting point used the same axial induction factor, and with the same approximations, estimated the tangential induction factor as

$$a' = \left[\frac{2}{\pi\sigma'\left(\frac{1-a}{\lambda_r} - \theta\right)} - 1\right] \tag{62}$$

Table III compares the speed and robustness of the various algorithms used during this study. Speed was quantified as the average number of function calls across the 800,000 (160,000 for the present method because only one starting point is necessary) simulations for the particular algorithm. Only simulations that were successful in converging were included in the average function call total. The failure rate denotes the percentage of simulations that did not converge. Arguably, the failure rate for some of the unbounded methods like Newton's method should be even higher because widely unrealistic values were still considered successful as long as the algorithm converged. The only difference between each method is the solution approach; the blade-element momentum formulation is identical. The results show that the present method is much more robust than the other methods (0 failures). As a secondary benefit, the present method is also the fastest of all tested methods (1.45X faster than the next fastest method, and 7.0X faster than the next most robust method). Iteration on the Reynolds number was not used in the present methodology. Its inclusion would approximately double the function calls for airfoils whose data included Reynolds number variation (actually slightly less than that because only a portion of the function is iterated on internally). Even in that case, the present algorithm's speed would be on par with the next fastest method. For the two-dimensional method, no one starting point was superior across all methods, but in general the second and third starting points that assumed optimal designs failed at a slightly higher rate than the others. For practical designs, the failure rate of the conventional methods would be much lower than these reported values, as simultaneous extremes in the parameters would be unlikely (e.g., low tip-speed ratio, low solidity, and large twist angle), and the inclusion of hub/tip losses tends to decrease the failure rates for most of the methods. However, such extreme combinations are likely to occur in the process of an optimization, thus these failure rates are more representative of the robustness of the methods for optimization applications.

Table III. Comparison in convergence speed and failure rate of several algorithms used to solve the BEM equations.

Algorithm	Avg. Function Calls	Failure Rate (%)
Fixed-Point	31.8	12.6
Newton	79.0	5.8
Steffensen	16.4	16.3
Powell Hybrid	72.3	16.2
Levenberg-Marquardt	92.3	8.8
Present Method	**11.3**	**0.0**

To further test the robustness of the present method, the clean S813 airfoil was studied on the same range of tip-speed ratios, solidities, and twist angles, but with a finer grid (200 x 200 x 200). This airfoil was chosen because, in the study by McWilliam and Crawford [4], they showed that the clean S813 airfoil [21] was particularly problematic for convergence. They conducted a three-dimensional parameter sweep across the same limits and noted that significant regions of the parameter space exhibited convergence instabilities when using Newton's method (fixed-point iteration showed even larger regions of instability). On the other hand, when using the proposed methodology of this paper *every* point in the design space converged to a solution. Perfect convergence for the present method was observed whether or not the airfoil data was used with linear interpolation or with a smooth spline fit. For the two-dimensional methods, using linear interpolation generally increased the failure rate slightly as compared to the reported values in Table III. Interestingly, when using the

present method for the studies in this section, the main bracket $(0, \pi/2]$ was valid for every simulation. The alternative brackets are generally only needed in extreme cases (e.g., large negative pitch, or extremely small tip-speed ratios).

5. CONCLUSION

This paper demonstrated a solution approach for the blade element momentum (BEM) equations that simplifies the typical two-dimensional fixed-point problem to a one-dimensional root-finding problem. This approach is equally valid for propellers or wind turbines, and allows any parameterization of the axial induction factor as long as it can be expressed as a function of the local inflow angle (ϕ). Although the implementation details may differ depending on the application and the different corrections to the BEM equations that are used, as long as a bracket can be found in a well-behaved region of the one-dimensional residual function, a solution to the BEM equations is guaranteed. For wind turbines applications and a typical BEM formulation, appropriate brackets were identified, and a provably convergent approach was demonstrated. Bounds bracketing the zero can be determined easily through one function call, and is for the vast majority of cases $(0, \pi/2]$. With a bracket determined, a suitable root-finding algorithm (e.g., Brent's method) will allow the BEM equations to be solved robustly (guaranteed convergence) and efficiently (with superlinear convergence).

REFERENCES

1. Manwell JF, McGowan JG, Rogers AL. *Wind Energy Explained*. 2nd edn., Wiley, 2009.
2. Hansen MOL. *Aerodynamics of Wind Turbines*. 2nd edn., Earthscan, 2008.
3. Burton T, Jenkins N, Sharpe D, Bossanyi E. *Wind Energy Handbook*. 2nd edn., Wiley, 2011.
4. McWilliam M, Crawford C. The behavior of fixed point iteration and Newton-Raphson methods in solving the blade element momentum equations. *Wind Engineering*, 2011; **35**(1):17–32, doi:10.1260/0309-524X.35.1.17.
5. Masters I, Chapman J, Orme J, Willis M. A robust blade element momentum theory model for tidal stream turbines including tip and hub loss corrections. *Proceedings of IMarEST-Part A-Journal of Marine Engineering and Technology*, 2011; **10**(1):25–35.
6. Maniaci DC. An investigation of WT_Pref convergence issues. *AIAA Aerospace Sciences Meeting*, AIAA 2011-150, 2011.
7. Platt A. WT Perf: Programming guide for v 3.05.00a-adp. *Technical Report*, National Renewable Energy Laboratory, October 2012.
8. Buhl ML. Personal communication. National Renewable Energy Laboratory, February 2013.
9. Buhl ML. A new empirical relationship between thrust coefficient and induction factor for the turbulent windmill state. *Technical Report NREL/TP-500-36834*, National Renewable Energy Laboratory, August 2005.
10. Brent RP. An algorithm with guaranteed convergence for finding a zero of a function. *The Computer Journal*, 1971; **14**(4):422–425, doi:10.1093/comjnl/14.4.422.
11. Ramsay RR, Hoffmann M, Gregorek G. Effects of grit roughness and pitch oscillations on the S815 airfoil: Airfoil performance report. *Technical Report*, The Ohio State University, December 1999.
12. Wilson R, Lissaman P, Walker S. Aerodynamic performance of wind turbines. *Technical Report*, Oregon State University, Corvallis, OR, 1976.
13. Kooijman H, Lindenburg C, Winkelaar D, van der Hooft E. DOWEC 6 MW pre-design: Aero-elastic modeling of the DOWEC 6 MW pre-design in phatas. *Technical Report DOWEC 10046_009*, Energy Research Center of the Netherlands, September 2003.
14. Jonkman J, Butterfield S, Musial W, Scott G. Definition of a 5-MW reference wind turbine for offshore system development. *Technical Report NREL/TP-500-38060*, National Renewable Energy Laboratory, Golden, CO, February

2009.

15. Abbott I, Von Doenhoff A. *Theory of Wing Sections: Including a Summary of Airfoil Data*. Dover publications, 1959.
16. Bertagnolio F, Sørensen N, Johansen J, Fuglsang P. Wind turbine airfoil catalogue. *Technical Report Risø-R-1280(EN)*, Risø National Laboratory, Roskilde, Denmark, August 2001.
17. Fuglsang P, Antoniou I, Sørensen N, Madsen H. Validation of a wind tunnel testing facility for blade surface pressure measurements. *Technical Report Risø-R-981(EN)*, Risø National Laboratory, Denmark, 1998.
18. Fuglsang P, Dahl K, Antoniou I. Wind tunnel tests of the Risø-A1-18, Risø-A1-21 and Risø-A1-24 airfoils. *Technical Report Risø-R-1112(EN)*, Risø National Laboratory, Denmark, June 1999.
19. Ramsay RR, Hoffmann M, Gregorek G. Effects of grit roughness and pitch oscillations on the S801 airfoil: Airfoil performance report. *Technical Report*, The Ohio State University, December 1999.
20. Ramsay RR, Hoffmann M, Gregorek G. Effects of grit roughness and pitch oscillations on the S810 airfoil: Airfoil performance report. *Technical Report*, The Ohio State University, December 1999.
21. Ramsay RR, Gregorek G. Effects of grit roughness and pitch oscillations on the S813 airfoil: Airfoil performance report. *Technical Report*, The Ohio State University, December 1999.
22. Ramsay RR, Janiszewska J, Gregorek G. Effects of grit roughness and pitch oscillations on the S825 airfoil: Airfoil performance report. *Technical Report*, The Ohio State University, December 1999.
23. Du Z, Selig M. A 3-D stall-delay model for horizontal axis wind turbine performance prediction. *1998 ASME Wind Energy Symposium*, AIAA-1998-21, 1998.
24. Eggers Jr AJ, Chaney K, Digumarthi R. An assessment of approximate modeling of aerodynamic loads on the UAE rotor. *Aerospace Sciences Meeting and Exhibit*, AIAA-2003-0868, 2003.
25. Viterna L, Janetzke D. Theoretical and experimental power from large horizontal-axis wind turbines. *NASA TM-82944*, National Aeronautics and Space Administration, Cleveland, OH. Lewis Research Center, September 1982.
26. Moriarty PJ, Hansen AC. AeroDyn theory manual. *Technical Report NREL/EL-500-36881*, National Renewable Energy Laboratory, December 2004.